Granular Matter (2008) 10:197–207
DOI 10.1007/s10035-007-0051-5

Fundamental study of thermal conduction in dry soils

T. S. Yun · J. C. Santamarina

Received: 20 June 2006 / Published online: 16 October 2007

Abstract The thermal conductivity of the different soil components—mineral, liquids and air—varies across two orders of magnitude. Two studies are implemented to explore the role of contacts in heat conduction in dry granular materials. The first set of experiments is designed to elucidate heat transfer at contacts, and it is complemented with a numerically based inversion analysis for different local and boundary conditions to extract proper material parameters. Then, the thermal conductivity of dry soils is measured at different packing densities to address the relevance of coordination number and particle shape effects. Together, both studies confirm the prevailing effect of contact quality and number of contacts per unite volume on heat conduction in granular materials. Interparticle contacts and the presence of liquids in pores play a critical role in heat transfer, and determine the ordered sequence of typical thermal conductivity values: $k_{\text{air}} < k_{\text{dry-soil}} < k_{\text{water}} < k_{\text{saturated-soil}} < k_{\text{mineral}}$.

Keywords Contact · Conduction · Diffusivity · Convection · Multiphase

T. S. Yun
School of Civil and Environmental Engineering,
790 Atlantic Drive, Atlanta, GA 30332-0355, USA

Present Address:
T. S. Yun
Department of Civil and Environmental Engineering,
Lehigh University, 13 East Packer Avenue,
Bethlehem, PA 18015, USA

J. C. Santamarina
Georgia Institute of Technology, Atlanta, GA 30332-0335, USA

J. C. Santamarina (✉)
Goizueta Chair School of Civil and Environmental Engineering,
790 Atlantic Drive, Atlanta, GA 30332-0355, USA
e-mail: jcs@gatech.edu

List of symbols

λ	heat loss coefficient (s^{-1})
ρ	mass density (g m^{-3})
ν	poisson ratio
A	area (m^2)
a	fitting parameter
A_c	contact area (m^2)
cn	interparticle coordination number
C_u	coefficient of uniformity
c_v	heat capacity (cal g^{-1} °C^{-1})
d	diameter (mm)
D	thermal diffusivity (m^2 s^{-1})
D_{50}	mean particle size (mm)
FR_d	larger particle size ratio
FR_{mass}	mass fraction
G	shear stiffness
I	electrical current (Ampere)
k	thermal conductivity (W m^{-1} K^{-1})
k_{eff}	effective thermal conductivity (W m^{-1} K^{-1})
L	loss factor (cal s^{-1}°C^{-1})
M	numerical modulus
N	normal force
n	porosity
p	fitting parameter
q	heat energy per unit time (cal s^{-1})
R	resistance (Ω)
S	saturation
T	temperature (°C)
t	time (min)
V	voltage (V)

1 Introduction

More than 98% of the earth's volume is at a temperature higher than 1,000°C, and the temperature of the earth core

Table 1 Factors that determine the thermal conductivity of soils

Factors	Features	Materials (References)
Mineralogy	As k_{solid} increases, k_{bulk} increases	Granite [23]
		Sand, glass bead and lead shot [24]
Particle size	Bigger particle supports higher k	Steel sphere [11]
		Silicon Nitrides [25]
		Clay–sand [26]
Applied pressure	As contact pressure increases, k increases	Stainless steel cylindrical particles: [7]
		Steel sphere [11]
		Aluminum and Stainless steel cylinder [27]
		Graphite composite [28]
		Aluminum and Stainless steel, spherical and cylindrical particle [29]
		Model prediction [30]
Density/Gradation	The decrease of porosity makes k increase	Cotton soil–sand [6]
		Bentonite [10]
		Quartz sand packs [24]
		Sand–clay, frozen–unfrozen [31]
Water content	Adding small amount of water to dry soil makes k improved	Cotton soil–sand [6]
		Bentonite [10]
	Higher water content presents higher k	Model prediction [19]
		Sand–clay, frozen–unfrozen [31]
Pore fluid	As k of saturating pore fluid increases, k_{bulk} increases	Gases and water [24]
		Air and water [32]

may exceed 5,000°C. This great geothermal dynamo has determined the geological history of the earth [1,2]. Heat flux in oceans and climate change are macro-scale manifestations of geothermal phenomena. Several geotechnical engineering problems involve the thermal properties of geomaterials; examples include thermal stabilization, foundation effects in permafrost regions, geomechanics of geothermal energy resource recovery, thermal storage, radioactive waste disposal, pavement performance in extreme climates, and the formation-destabilization of methane hydrates in subseafloor sediments (see for example [3,4]).

The thermal conductivity k of the different soil components varies across two orders of magnitude: $k_{mineral} > 3\,W\ m^{-1}\ K^{-1}$, $k_{water} = 0.56\,W\ m^{-1}\ K^{-1}$ (at 0°C) and $k_{air} = 0.026\,W\ m^{-1}\ K^{-1}$. While the thermal conductivity is high in minerals, it is quite low in dry soils made of the same minerals, in fact $k_{dry\text{-}soil} < 0.5\,W\ m^{-1}\ K^{-1}$ in most cases. This observation suggests that the main heat transfer path in particulate materials is through solid particle contacts.

There are three heat transfer mechanisms: conduction prevails in solids, convection in fluids, and radiation does not require a material medium. Given the role of packing density and effective stress on thermal conductivity in dry soils, the solid particle-to-particle contact appears as the most effective path for heat transfer [5–7]. On the other hand, conduction through the gas phase and radiation has minute effects, until convection becomes effective when the mean particle size is $D_{50} > 6\,mm$ permitting fluid currents in pores and through the porous network [5,8,9]. The addition of water to a granular material increases its thermal conductivity significantly [6,10,11]. Selected previous studies on thermal conduction in particulate materials are reviewed in Table 1.

Semi-empirical correlations extracted from several soil thermal conductivity data sets are summarized in Table 2. In addition, theoretical mixture models developed to predict the thermal properties of solid-fluid mixtures are summarized in Table 3. The theoretical prediction of thermal conductivity is based on the mixture geometry, the properties of each phase and the volumetric fractions.

This study is designed to gain further insight into particle-level mechanisms that govern heat transfer in particulate materials. A sequence of experimental and numerical studies at the particle scale and at the macroscale follows.

Table 2 Thermal conductivity of soils—Semi-empirical models

Reference	Features
Johansen's correlation[a] 1975	Correlation with particle size, saturation, and particle conductivity. $k = (k_{sat} - k_{dry})K_e + k_{dry}$ K_e = Kersten number. Each parameter has its own empirical relations (see Andersland and Ladanyi, 2004 for details) $k_{dry}(W/mK) = \frac{0.137\rho_{dry}+64.7}{\rho_{solid}-0.947\cdot\rho_{dry}} \pm 20\%(\rho \text{ in kg m}^{-3})$ $k_{dry}(W/mK) = 0.039n^{-2.2} \pm 25\%$ for crushed rock materials
[33]	Correlation with saturation. $S = \lambda_1[\sinh(\lambda_2 k + \lambda_3) - \sinh(\lambda_4)]$ S = saturation, k = thermal conductivity (Btu in ft^{-2} h^{-1} °F^{-1}) $\lambda_1 \sim \lambda_4$ = coefficients fitted.
[34]	$k_{dry} = 0.025 + 0.238\rho_{dry} - 0.193\rho_{dry}^2 + 0.114\rho_{dry}^3$ for mineral/organic soil ρ_{dry}= dry density (< 2 g cm^{-3})

[a]Summarized in [35]

Table 3 Theoretical thermal conductivity mixture models.

Model	Effective thermal conductivity		References
Series	$k_{eff} = \left[\sum_i \frac{n_i}{k_i}\right]^{-1}$	Summarized in [36]	
Parallel	$k_{eff} = \sum_i n_i \cdot k_i$		
Geometric mean	$k_{eff} = k_i^{n_i}$		[37]
Hashin and Shtrikman Boundary	$k_{eff} = k_1\left[1 + \frac{3n_2(k_2-k_1)}{3k_1+n_1(k_2-k_1)}\right]$	Lower: 1 = solid, 2 = pore, upper: 1 = pore, 2 = solid	[38]
Self consistent method	$k_{eff} = \frac{1}{3}\left[\frac{1-n}{2k_{eff}+k_m} + \frac{n}{2k_{eff}+k_a}\right]^{-1}$		[19,39]
Cubic cell	$\frac{1}{k_{eff}} = \frac{\beta-1}{k_a\cdot\beta} + \frac{\beta}{k_a\cdot(\beta^2-1)+k_m}$ where $\beta = \left[\frac{1}{1-n}\right]^{1/3}$ dry soil		[40]

2 Thermal conduction in a 1-D granular chain

Heat transfer between particles is explored next through complementary experimental and numerical techniques.

2.1 Experimental study

This study centers on the long column of spherical metal particles shown in Fig. 1. The 15 aluminum-bronze spheres (Alloy 630–25.4 mm diameter, thermal conductivity $k = 39.1$ W m^{-1} K^{-1}, thermal diffusivity $D = 136.8 \cdot 10^{-7}$ m^2 s^{-1}) are vertically aligned within a wooden guide (thermal conductivity $k \cong 0.1$ W m^{-1} K^{-1}, thermal diffusivity $D \cong 0.5 \cdot 10^{-7}$ m^2 s^{-1}). The metal rod as a heat source (103°C to 107°C) is brought into contact with the bottom sphere at time $t = 0$. The whole system is in air at room temperature $T \sim 20$°C. Each particle has a small perforation (1.8 mm diameter) to host a thermocouple (TP-29, B&K Precision) that monitors the core temperature. Values of temperature in the 15 particles and at the source are logged every 10 s until the temperature reaches equilibrium at all particles.

Six contact and boundary conditions are tested (Fig. 2):

- Reference column (O): Particles are vertically aligned without any contact modification or special boundary condition.
- Contact Retardation (RO): A single sheet of filter paper (medium porosity) is placed between particles to hinder heat transfer at contacts.
- Load (LO): A force of 160 N is applied at the top to improve interparticle contact coupling. Assuming that the 'contribution area' to a particle is $(2R)^2$ in a simple cubic

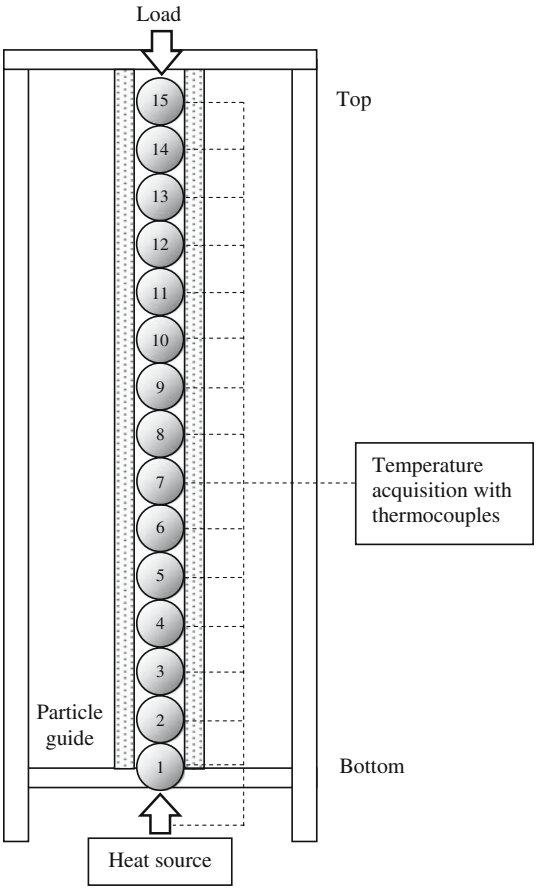

Fig. 1 Test design for the study of heat transfer in a granular chain. The temperature at the core of each particle is monitored with an embedded thermocouple while heat is applied to the bottom particle

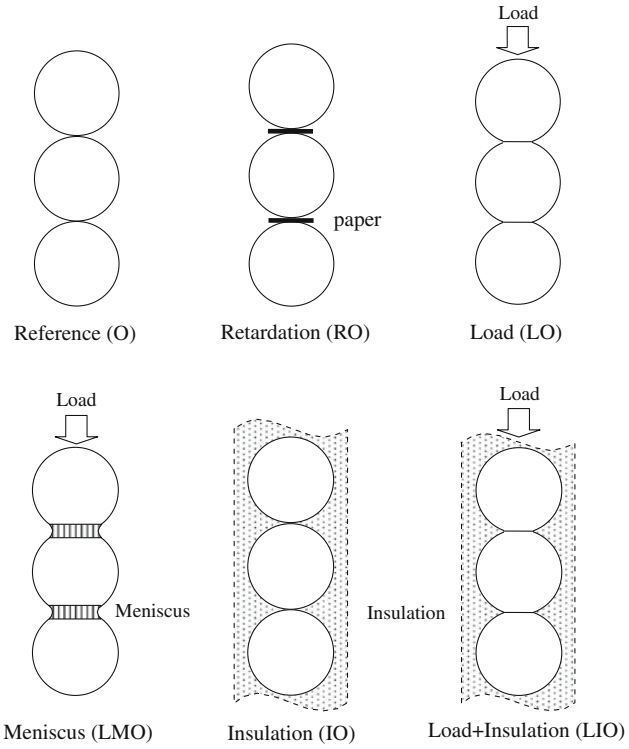

Fig. 2 Particle column—Test conditions designed to attain different contact quality and heat loss to the surrounding medium

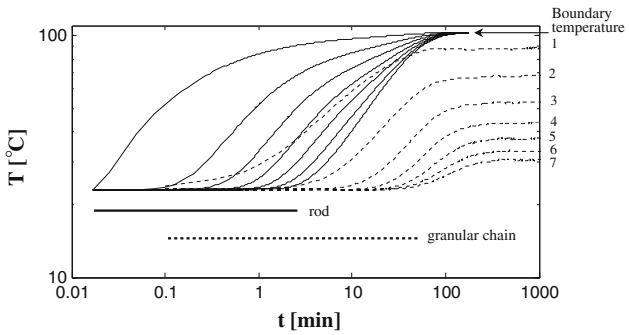

Fig. 3 Temperature evolution for particles #1–7 in granular column with load and insulation (LIO). The *solid lines* indicate the temperature changes calculated for a continuous 1D-column of constant cross section made of the same material for the particles

configuration, the nominal equivalent effective stress is $\sigma = N^{sc}/4R^2 \sim 250$ kPa.

- Load-Meniscus (LMO): The interparticle contact areas are purposely enlarged with a metal patch ($d_{contact} \sim 12$ mm, S-50, Devcon Inc., $k = 2.3\,W\,m^{-1}\,K^{-1}$) and the 160 N vertical force is applied before the metal patch cures.
- Boundary Insulation (IO or LIO): The entire column is insulated with a foam sealant to reduce radiation and convection heat loss. Tests are repeated with (LIO) and without (IO) the 160 N axial force.

The temperature-time histories at selected particles #1–7 are presented as dotted lines in Fig. 3 for the loaded column with insulation at contacts LIO. The complete dataset is documented in [12]. The temperature of the bottom particle that is in direct contact with the heat source increases first, followed by the increase in temperature of upper particles. For comparison, the solid lines represent the temperature evolution calculated at the same distances from the heat source for the case of a continuous 1D rod of constant cross section, made of the same material as the particles, assuming no heat loss to the surrounding medium. Clearly, conduction is more effective in the rod than in the particle column. Furthermore, the equilibrium temperature in the rod reaches the boundary temperature at all distances from the source (103°C). However, the final, steady-state temperature in each particle does not converge to the same asymptotic value; in fact, the equilibrium temperature decreases from the bottom to the top particle; this implies heat loss to the surrounding medium along the 1-D particle column.

Figure 4 compares temperature time histories for particle #3 under different test conditions. The following observa-

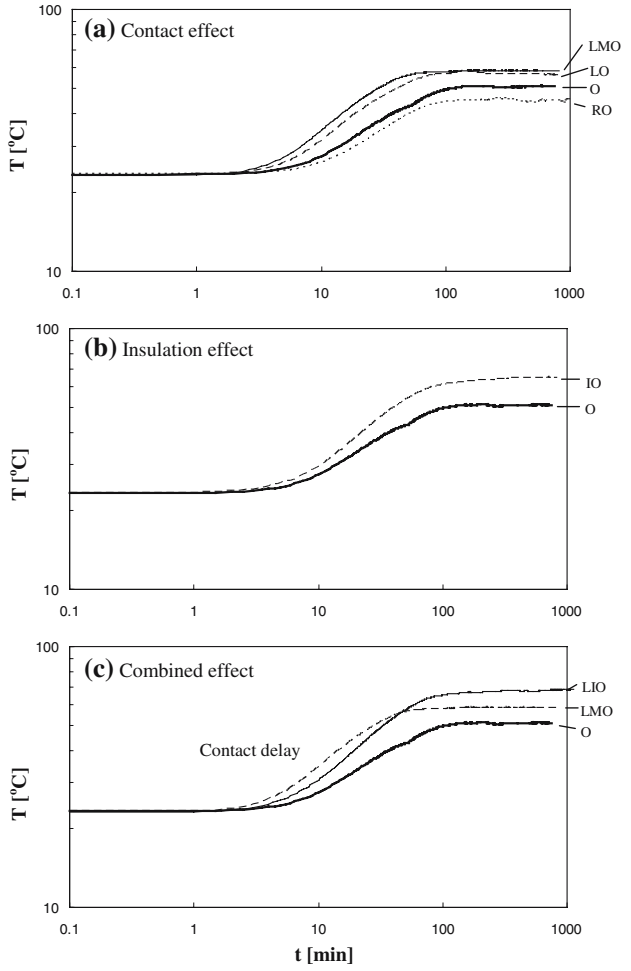

Fig. 4 Temperature time history comparison (3rd particle from bottom)—Heat transfer under different contact and boundary conditions. **a** Contact effect: the large contact area (LO and LMO) causes early temperature rise and higher equilibrium temperature than RO. **b** Insulation effect: Heat loss reduction by insulation leads to increased conduction and higher equilibrium temperature. **c** Combined effect: larger contact area (LMO) supports earlier temperature increase while surface insulation (LIO) supports higher equilibrium temperatures than LMO

tions can be made by comparing trends for different contact conditions against results for the reference column (O: thick solid line):

- Contact effects (Fig. 4a). The initial temperature evolution is delayed when poor contact conditions prevail (RO: dotted line). Furthermore, the final steady-state temperature for RO is lower than the reference (O). On the other hand, normal contact load enhances thermal conduction, and leads to a higher equilibrium temperature (LO: dashed line). The addition of a medium of intermediate conductivity at contacts causes faster and steeper thermal evolution, and higher equilibrium temperature (LMO: solid line). Therefore, particle contact conditions (including water at contacts in soils) determine both the rate of heat transfer and the equilibrium temperature.
- Insulation effects (Fig. 4b). Convective air circulation and radiation heat losses are reduced by shielding particle surfaces. Heat loss reduction leads to increased conduction and higher equilibrium temperature (IO—Note that there is heat loss even with the addition of insulation).
- Combined effects (Fig. 4c). Heat loss and contact resistance have different affects on the measured time histories. While heat loss due to boundary insulation is mainly responsible for the equilibrium temperatures, interparticle contact conditions determine the rate of transfer and the early stages of heating. For example, the temperature rise in the presence of conductive menisci (LMO: dashed line) precedes temperature rise in the insulated and loaded system (LIO: solid line) during transient conditions, even though particles for LIO reach higher equilibrium temperatures.

3 Equivalent rod: numerically-based inversion analysis

The data gathered in all six cases are numerically modeled assuming an equivalent 1-D rod model. Energy conservation implies that the rate of outflow heat q_{out} (cal s^{-1}) is the sum of the rate of inflow heat q_{in}, the power used for heating the material, and the rate of heat loss. Thus, the heat flow per unit time

$$\underbrace{q_{\text{out}}}_{\substack{\text{Outflow}\\ \text{heat rate}}} = \underbrace{q_{\text{in}}}_{\substack{\text{Inflow}\\ \text{heat rate}}} - \underbrace{c_{\text{v}} \cdot \rho \cdot dx \cdot A \cdot \frac{dT}{dt}}_{\substack{\text{Power used for}\\ \text{material heating}}} - \underbrace{L \cdot T^*}_{\substack{\text{Rate of}\\ \text{Heat loss}}} \quad (1)$$

The parameters in this equation are heat capacity c_v(cal $g^{-1}{}^{\circ}C^{-1}$), mass density ρ(g m^{-3}), distance x (m), area A(m^2), temperature T(°C), and the loss factor L(cal $s^{-1}{}^{\circ}C^{-1}$) that relates the heat loss to the instantaneous temperature difference T^* between a particle and the surrounding medium herein assumed at constant temperature. Given a differential element length dx,

$$-\frac{dq}{dx} = c_{\text{v}} \cdot \rho \cdot A \cdot \frac{dT}{dt} + \frac{L}{dx} \cdot T^* \quad (2)$$

The rate of heat transfer by conduction is $q = -k \cdot A \cdot (dT/dx)$. Therefore, Eq. 2 results in

$$\frac{d^2T}{dx^2} = \frac{c_{\text{v}} \cdot \rho}{k} \cdot \frac{dT}{dt} + \frac{L}{k \cdot A} \cdot \frac{T^*}{dx} \quad (3)$$

Rearranging

$$\frac{dT}{dt} = D \cdot \frac{d^2T}{dx^2} - \lambda \cdot T^* \quad (4)$$

where $\lambda = L/(dx \cdot A \cdot c_{\text{v}} \cdot \rho)$ is taken as a constant for the purpose of this study. In explicit finite difference form, Eq. 4

can be written as:

$$T_{i,j+1} = M \cdot T_{i+1,j} + (1 - 2M - \lambda \cdot \Delta t) \cdot T_{i,j} + M \cdot T_{i-1,j} + \lambda \cdot \Delta t \cdot T_{\text{sur}} \quad (5)$$

where i and j are indices for spatial and temporal scales, T_{sur} is the surrounding room temperature and the numerical modulus is $M = D \cdot \Delta t / \Delta x^2$.

Equation 4 captures the interplay between thermal diffusivity $D(\text{m}^2\ \text{s}^{-1})$ and loss $\lambda(\text{s}^{-1})$. In particular, higher thermal conduction and smaller loss λ have a similar effect on the early temperature time history of each particle. Therefore, the thermal diffusivity D and the loss coefficient λ must be simultaneously fitted to a complete set of thermal time histories in order to extract the correct thermal diffusivity D value for the equivalent rod. A least square inversion is implemented. The error in temperature is computed in log-scale to emphasize early low values. The corresponding error for the ith measurement and the total L_2 error norm are

$$e_i = \log\left[\frac{T_i^{\text{measured}}}{^{\text{o}}\text{C}}\right] - \log\left[\frac{T_i^{\text{predicted}}}{^{\text{o}}\text{C}}\right] = \log\left[\frac{T_i^{\text{measured}}}{T_i^{\text{predicted}}}\right] \quad (6)$$

$$L_2 = \left[\sum_i e_i^2\right]^{0.5} \quad (7)$$

The iterative algorithm starts with in initial guess of D and λ, and continues until the inverted values of D and λ are identified for the minimum L_2. Figure 5 shows measured and predicted time series for two tests (IO and LIO). The equivalent 1-D rod model adequately captures experimental results. The evaluated thermal diffusivity and loss coefficient values are summarized in Table 4. Numerical results corroborate previous experimental observations. In particular, thermal diffusivity D decreases when poor contact conditions prevail (RO); on the contrary, D increases when heat can be more easily transported across larger contact areas attained by either loading (examples: LO and LIO), cementation or water menisci (LMO); and loss reduction by peripheral insulation prevents heat loss and leads to higher heat conduction (i.e., higher D and smaller λ - IO and LIO).

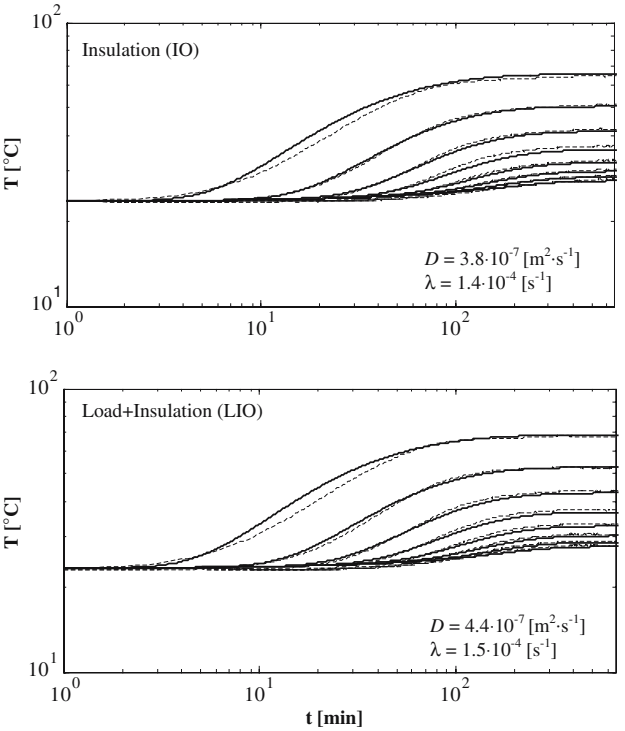

Fig. 5 Measured and fitted thermal time histories—shown for selected particles. *Dotted line* experiment; *solid line* numerical simulation using the equation for 1-D rod model

The thermal diffusivity in the particle column is only 1.2 to 4.8% of the thermal diffusivity in the metal that makes the particles ($D \cong 1.7$ to $6.5 \cdot 10^{-7}$ m^2 s^{-1} for all columns made of spheres, while $D = 136.8 \cdot 10^{-7}$ m^2 s^{-1} for solid Aluminum-bronze). Finally, it is worth noting that the thermal diffusion in the column is much higher than in either the wooden guide ($D \cong 0.5 \cdot 10^{-7}$ m^2 s^{-1}) or the insulating foam ($D \cong 1 \cdot 10^{-7}$ m^2 s^{-1} estimated from the literature). Hence, the assumed analytical model in Eq. 4 adequately captures the tested physical model.

4 Thermal conduction in dry soils

Contact quality and the number of contacts per particle depend on the packing density, particle shape and grain

Table 4 Inverted thermal diffusivity D and loss coefficient λ values for the different test conditions

Test	L_2 error	$D(\text{m}^2\ \text{s}^{-1}) \times 10^{-7}$	$\lambda(\text{s}^{-1}) \times 10^{-4}$
Reference column (O)	4.50	2.6	2.4
Hindered contact (RO)	2.25	1.7	2.7
Contact load (LO)	2.66	5.0	2.9
Load with menisci (LMO)	13.33	6.5	2.8
Insulation (IO)	0.86	3.8	1.4
Insulation and contact load (LIO)	0.89	4.4	1.5

size distribution. Their effects on thermal conductivity are explored in this section using selected sands and the thermal needle probe technique. The index properties of the selected sands are summarized in Table 5 and the measurement procedure is described next. Then, two experimental studies are conducted with careful porosity control.

4.1 Measurement of thermal conductivity

The needle probe consists of a heating wire and a thermocouple installed within a 1 mm diameter metal needle (Thermal Logic). Heat is generated by imposing a DC current through the heating wire, while the temperature evolution within the needle is monitored using the thermocouple (Fig. 6): the higher the thermal conductivity of the medium, the higher the rate of heat dissipation and the lower the rate of temperature increase detected with the thermocouple. The electric current I is related to the voltage drop V_{ref} across a reference resistor R_{ref} placed in series with the heating wire,

$$I = V_{\text{ref}}/R_{\text{ref}} \tag{8}$$

Then, the input power Q is

$$Q = I^2 \cdot R_{\text{m}} = \left(\frac{V_{\text{ref}}}{R_{\text{ref}}}\right)^2 \cdot R_{\text{m}} \tag{9}$$

where R_m is the resistance of the heating wire. The early portion of the temperature time series is affected by the needle-soil coupling while specimen boundaries perturb the long-time data. Therefore, the thermal conductivity is obtained from the linear, central portion of the temperature versus log time plot. The thermal conductivity is computed as (derivation in [5]):

$$k = \frac{Q}{4\pi} \cdot \frac{\ln(t_2/t_1)}{(T_2 - T_1)} = \left(\frac{V_{\text{ref}}}{R_{\text{ref}}}\right)^2 \cdot \frac{R_{\text{m}}}{4\pi} \cdot \frac{\ln(t_2/t_1)}{(T_2 - T_1)} \tag{10}$$

This methodology is valid for homogeneous, isotropic materials (details can be found in [13,14]).

4.2 Experimental study #1: Porosity control by densification

In this first study, sand is air-pluviated into a zero lateral strain cell (diameter = 152.5 mm, height = 155 mm). The thermal needle probe is then vertically inserted into the soil. The temperature is logged every 0.5 s for 2 min (Agilent multimeter 34401A). The voltage drop V_{ref} remains relatively constant throughout the test and it is recorded to calculate the input energy. Measurements are repeated every 10 min. Once three measurements are completed, the specimen is densified on a shaking table to attain gradual reductions in porosity (ASTM D4253–93; shaking frequency = 50 ∼ 60 Hz).

Measured thermal conductivity values are plotted against porosity in Fig. 7. Following the particle-level studies in the previous section, it is inferred that the increase in thermal conductivity with decreasing porosity reflects the increase in the number of contacts per volume and possible improvements in conduction efficiency (Note that the number of contacts per volume is directly related to the coordination number in packings of monosized particles). Particle shape affects thermal conductivity through the packing density (for example, compare the data for round Ottawa 20–30 sand with angular blasting sand in Table 5): particle irregularity leads to increased porosity, and lower interparticle coordination [15]. In turn, lower porosity correlates with higher thermal conductivity. Therefore, a correlation between porosity in dry soils and thermal conductivity already captures the effect of particle shape on the number of contacts per unit volume. Note, however, that particle irregularity makes the stiffness of the granular skeleton more sensitive to the state of the stress due to enhancement in contact area [15]. A similar trend is anticipated for thermal conduction.

4.3 Experimental study #2: Porosity control through granular mixture

Results for the well graded, crushed sand-I and the poorly graded crushed sand-II suggest that well graded sands attain lower porosities and higher k values (Fig. 7). Consequently, there is improved heat transfer and higher thermal conductivity. This is further explored using mixtures of small particles that can fill the pore space between large particles, and increase the packing density and number of contacts per volume. Published studies show that the minimum porosity can be obtained for a mass fraction of small particles $\text{FR}_{\text{mass}} \sim 30$–$40\%$, and that the larger size ratios $\text{FR}_{\text{d}} = D_{\text{large}}/D_{\text{small}}$ produce lower porosity and higher mixture density [16,17].

F110 sand and Ottawa 20/30 sand are selected for this study. Both have low coefficient of uniformity C_u and high roundness (Table 5). The size ratio $\text{FR}_{\text{d}} = (D_{50})_{\text{ottawa}}/(D_{50})_{\text{F110}} \cong 6$. The two sands are mixed at different mass fractions and each mixture is placed in the test cell by funneling to prevent segregation (cell diameter = 83.7 mm and height = 103 mm). Then, the thermal needle probe is inserted into the specimen and the temperature is logged every 0.5 s for 2 min. Measurements are repeated several times for each specimen.

The thermal conductivity and the porosity of each mixture is plotted versus the volume fraction in Fig. 8a. The maximum thermal conductivity is measured for the specimen with a mass ratio $\text{FR}_{\text{mass}} \cong 40\%$ which has the minimum porosity. The thermal conductivity-versus-porosity trend for all mixtures is explored in Fig. 8b which confirms the inverse relationship between conductivity and porosity.

Table 5 Tested soil properties

Features	Ottawa 20/30 sand	Ottawa F110 sand	Blasting sand	Crushed sand-I	Crushed sand-II	Crushed sand-III
Mineral	Quartz	Quartz	Quartz	Granite, gneiss	N/A	Granite
Porosity, n_{max}	0.426	0.459	0.506	0.482	0.476	0.441
Porosity, n_{min}	0.334	0.349	0.411	0.345	0.351	N/A
D_{50} (mm)	0.72	0.12	0.71	0.33	0.52	0.3
D_{10} (mm)	0.65	0.081	0.42	N/A	N/A	N/A
C_u	1.15	1.62	1.94	5.5	2.3	3.2
C_c	1.02	0.99	0.94	N/A	N/A	N/A
G_s	2.65	2.65	2.65	N/A	N/A	N/A
Roundness	0.9	0.7	0.3	0.1	0.5	0.2
Sphericity	0.9	0.7	0.55	0.6	0.9	0.9

Data source: [15]

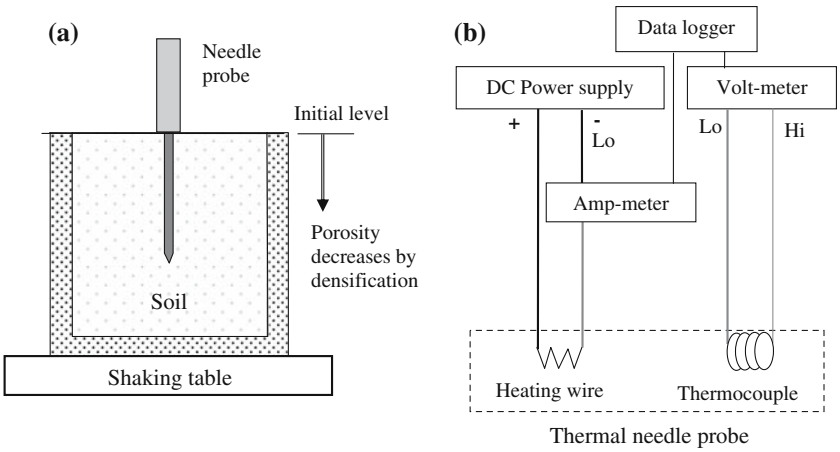

Fig. 6 Experimental study of thermal conductivity in dry sands. **a** Dry sand is placed in the cell. Vibration by means of a shaking table is used to control the porosity. The thermal needle probe is inserted into the specimen to obtain the thermal conductivity. **b** Needle probe and peripheral electronics. The heating wire and thermocouple are embedded inside the needle probe. The peripheral electronics are connected to apply the DC voltage and to measure the imposed current and the output voltage from thermocouple

5 Discussion

Figure 9 shows all measured thermal conductivity values (studies #1 and #2) plotted versus porosity, and trends predicted with theoretical and empirical thermal conductivity models. Semi-empirical models in Table 2 adequately fit experimental data (Fig. 9b). Theoretical models (Table 3) are computed assuming that the thermal conductivity of quartz and air are $k_{\text{mineral}} = 8.4$ W m^{-1} K^{-1} and $k_{\text{air}} = 0.026$ W m^{-1} K^{-1}. The thermal conductivity of the tested sands drops sharply from the thermal conductivity of quartz (Note that the y-axis is in log scale in Fig. 9a and b). The volume fraction model (equivalent to the Complex Refractive Index Method, CRIM) and the log-model are fitted as:

$$k_{\text{eff}} = \left[n \cdot k_{\text{air}}^{s} + (1-n) \cdot k_{\text{mineral}}^{s}\right]^{1/s} \quad (11)$$

with a value $s = -0.25$

$$k_{\text{eff}} = -a \cdot \ln(n) + p \quad (12)$$

where values $a = 0.291$ W m^{-1} K^{-1} and $p = 0.026$ W m^{-1} K^{-1}. Given the correlation between porosity and interpaticle coordination cn, these expression can be rewritten in terms of cn to highlight the relevance of contacts on thermal conduction (for example: $cn = 12(1-n)$; other correlations can be found in [17]).

Most models overestimate the thermal conductivity of dry sands except the Series and Hashin-Shtrikman lower bound models. Therefore, the comparison between theoretical and experimental results suggest that effective thermal conductivity models for particulate materials must not only consider volumetric fractions and the bulk conductivity of each

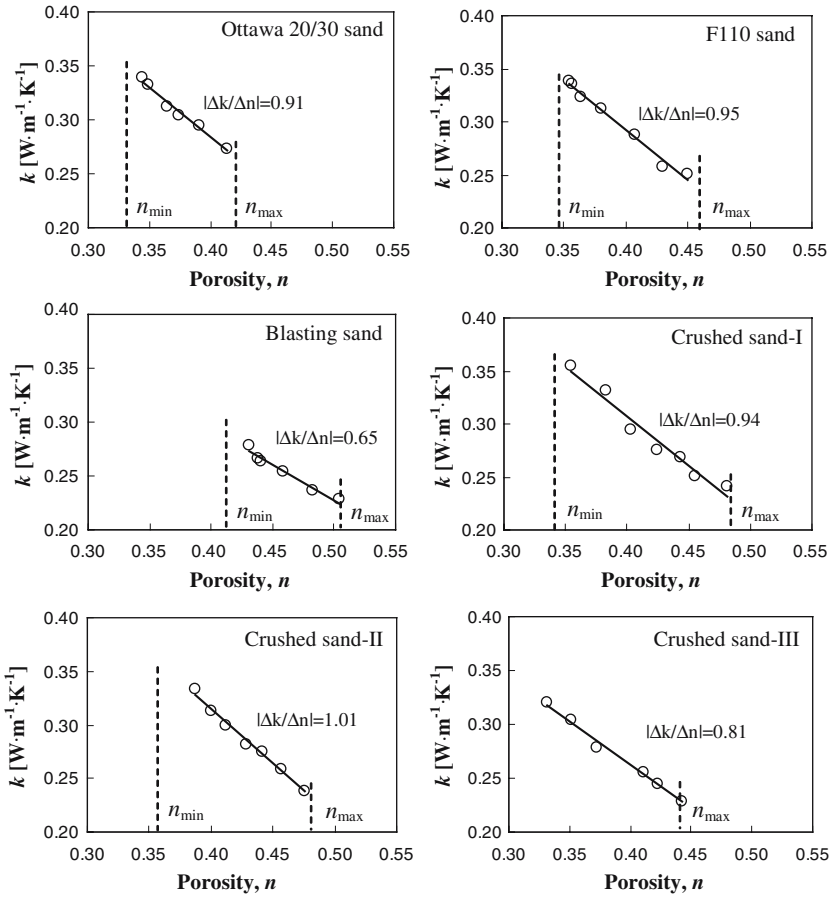

Fig. 7 Changes in thermal conductivity with porosity. Maximum and minimum porosities are calculated from maximum and minimum void ratios $n = e/(1 + e)$. Refer to Table 5. The thermal conductivity increases linearly with decreasing porosity in all cases

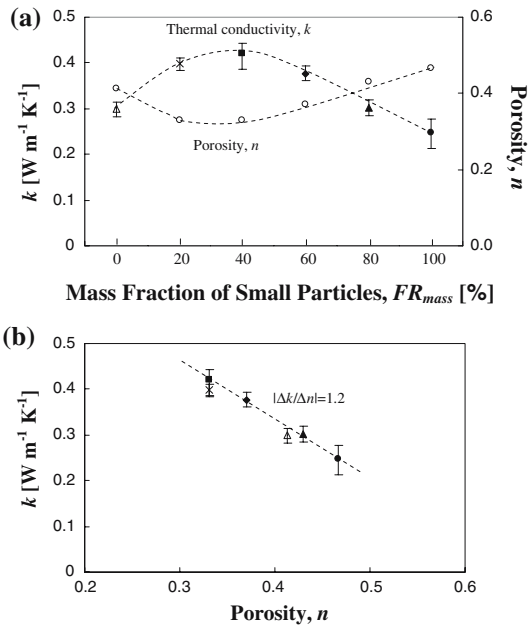

Fig. 8 Granular mixtures. Porosity control through the volume fraction of small particles. $FR_{\mathrm{d}} = D_{50\,\mathrm{large}}/D_{50\,\mathrm{small}}) \cong 6$. **a** The maximum thermal conductivity is obtained at minimum porosity (small particle fraction $\sim$ 40%). **b** Regardless of porosity changes with $\mathrm{FR_{mass}}$, the thermal conductivity increases linearly with decreasing porosity

phase but also the inherent presence of contacts in particulate materials [18,19].

Particle-level conduction mechanisms in granular materials have long been recognized [11,20] (Fig. 10):

- Conduction in the solid particle: Heat propagates within the mineral that makes the particle.
- Solid-to-solid conduction through the contact area.
- Solid–fluid–solid conduction: Heat is conducted from the particle into the fluid and back into neighboring particles. This conduction path is especially relevant in partially saturated soils with pendular water.
- Conduction in pore fluid: Heat conduction takes place through the fluid within the porous network.
- Convection: The fluid near particles warms up and initiates natural convection currents. This heat transfer mode is relevant when $D_{50} \geq 6$ mm [8].
- Radiation at interparticle contacts: heat propagation takes place by radiation across the gap between contacting particles.
- Radiation from the particle surface into the surrounding medium [21]. The penetration depth is inversely proportional to the material density (e.g., few centimeters in water and tens of meters in air).

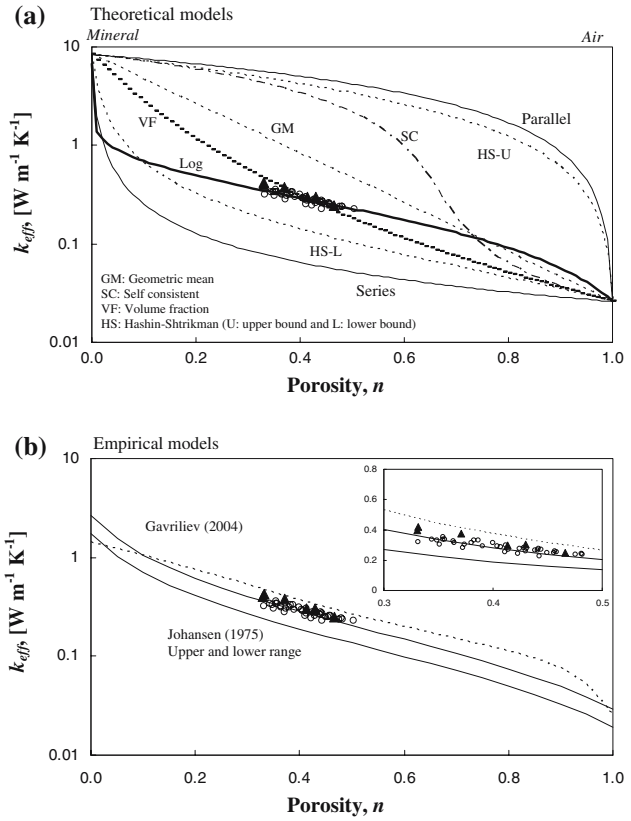

Fig. 9 Thermal conductivity versus porosity. Experimental results shown as *open circles* (39 measurements-6 sands) and *triangles* (mixtures). Model predictions are shown as *lines*

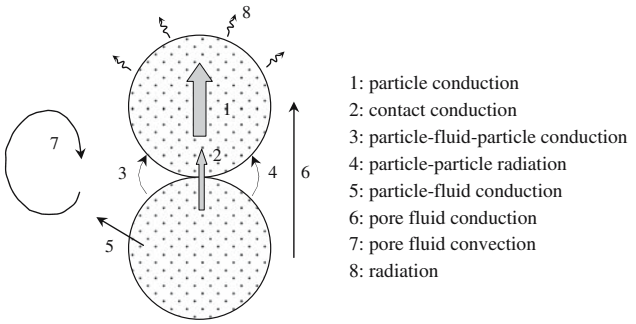

Fig. 10 Summary of heat transfer paths in particulate materials

Particle-level measurements, macro-scale tests and numerical simulations in this study show that heat flux through contacts plays a preponderant role on the effective thermal conductivity in dry soils. The contact area A_c depends on the contact normal force N. For a Hertzian contact between two Spherical particles, A_c is [22]

$$A_c = \pi \left[\frac{3(1-\nu)N}{8G\sqrt{r}} \right]^{\frac{2}{3}} \tag{13}$$

where ν and G are the Poisson ratio and shear stiffness of the mineral that makes the particles. This explains the role of effective stress on thermal conductivity in granular materials at constant packing [7,11]. Furthermore, experimental results suggest that contact level conduction increases not only by loading but any other mechanism that enhances the effective contact area, including flattening of surface roughness, cementation, creep/diagenesis and pendular water.

6 Conclusions

There are several heat transport processes in granular materials. The quality of interparticle contacts and the number of contacts per unit volume govern thermal conduction in dry soils. The presence of liquids or cementing agents at contacts, and larger contact areas (due to either loading, creep, or diagenesis) enhance thermal conduction.

The particle-level analysis of heat transfer explains the ordered sequence of typical thermal conductivity values: $k_{air} < k_{dry\text{-}soil} < k_{water} < k_{saturated\text{-}soil} < k_{mineral}$.

There are competing effects between heat transfer within the granular skeleton and heat loss to the pore space. Improvements in interparticle contacts result in higher thermal gradient with the surrounding medium eventually leading to higher heat transfer to the pore space.

The development of effective thermal conductivity models in particulate materials must recognize that interparticle contacts play a decisive role in heat transfer.

Porosity is the most important macroscale parameter on the thermal conductivity of dry soils: the thermal conductivity of the dry soil linearly increases as the porosity decreases. Low porosity implies high interparticle coordination at the particle scale. Round particles and well-graded soils tend to attain denser packing, higher number of contacts per unit volume and higher thermal conductivity than angular particles.

Acknowledgements This research was conducted by the authors at the Georgia Institute of Technology. Support was provided by the Goizueta Foundation at Georgia Tech and the Joint Industry Project administrated by ChevronTexaco.

References

1. Stein, C.A., Stein, S.: A model for the global variation in oceanic depth and heat flow with lithospheric age. Nature **359**(6391), 123 (1992)
2. Verhoogen, J.: Energetics of the earth, p. 139. National Academy of Sciences, Washington, DC (1980)
3. Miller, D.L.: Thermal design considerations in frozen ground engineering: a State of the Practice Report in Temperature Monitoring/Ground Thermometry, Prepared by the Technical Council on Cold Region Engineering of the American Society of Civil Engineers. Krzewinski, T.G., Tart, R.G. (eds.) pp. 53–71, ASCE: New York (1985)

4. Joshi, R.C., Achari, G., Horsfield, D., Nagaraj, T.S.: Effect of heat transfer on strength of clay. J. Geotech. Eng. **120**(6), 1080–1088 (1994)
5. Carslaw, H.S., Jaeger, J.C.: Conduction of Heat in Solids, p. 510. Clarendon Press, Oxford (1959)
6. Singh, D.N., Devid, K.: Generalized relationships for estimating soil thermal resistivity. Exp. Thermal Fluid Sci. **22**, 133–143 (1992)
7. Vargas, W.L., McCarthy, J.J.: Heat conduction in granular materials. AIChE J. **47**(5), 1052–1059 (2001)
8. Thalmann, R.E.: Thermal Conductivity of Dry Soils. University of Kansas, Lawrence, KS (1950)
9. Lambert, M.A., Fletcher, L.S.: Review of models for thermal contact conductance of metals. J. Thermophys. Heat Transf. **11**(2), 129–140 (1997)
10. Tang, A.-H., Cui, Y.-J., Le, T.-T.: Thermal properties of compacted bentonites. Can. Geotech. J. (2006) (in press)
11. Weidenfeld, G., Weiss, Y., Kalman, H.: A theoretical model for effective thermal conductivity (ETC) of particulate beds under compression. Granular Matter. **6**, 121–129 (2000)
12. Yun, T.S.: Mechanical and thermal study of hydrate bearing sediments, in School of Civil and Environmental Engineering, p. 179. Georgia Institute of Technology, Atlanta (2005)
13. Manohar, K., Yarbrough, D.W., Booth, J.R.: Measurement of apparent thermal conductivity by the thermal probe method. J. Test. Eval. **28**(5), 345–351 (2000)
14. Standard test method for determination of thermal conductivity of soil and soft rock by thermal needle probe procedure (ASTM D 5334–00)
15. Cho, G.C., Dodds, J., Santamarina, J.C.: Particle shape effects on packing density, stiffness and strength—natural and crushed sands. J. Geotech. Geoenviron. Eng. **132**(5), 591–602 (2006)
16. Guyon, E., Oger, L., Plona, T.J.: Transport properties in sintered porous media composed of two particle size. J. Appl. Phys. D: Appl. Phys. **20**, 1637–1644 (1987)
17. Santamarina, J.C., Klein, K.A., Fam, M.: Soils and Waves—Particulate Materials Behavior, Characterization and Process Monitoring, p. 488. Wiley, New York (2001)
18. Fletcher, L.S.: Recent developments in contact conductance heat transfer. J. Heat Transf. **110**, 1059–1070 (1988)
19. Tarnawski, V.R., Leong, W.H., Gori, F., Buchan, G.D., Sundberg, J.: Inter-particle contact heat transfer in soil systems at moderate temperatures. Int. J. Energy Res. **26**, 1345–1358 (2002)
20. Yagi, S., Kunii, D.: Studies on effective thermal conductivity in Packed Bed. AIChE J. **3**(3), 373–381 (1957)
21. Aduda, B.O.: Effective thermal conductivity of loose particulate systems. J. Mater. Sci. **31**, 6441–6448 (1996)
22. Williams, J.A.: Engineering tribology, p. 488. Oxford Science Publ., Oxford (1994)
23. Cote, J., Konrad, J.M.: Thermal conductivity of base course material. Can. Geotech. J. **42**, 61–78 (2005)
24. Woodside, W., Messmer, J.H.: Thermal conductivity of porous media. I. Unconsolidated sands. J. Appl. Phys. **32**(9), 1688–1698 (1961)
25. Ye, J., Kojima, N., Furuya, K., Munakata, F., Okada, A.: Microthermal analysis of thermal conductance distribution in advanced silicon nitrides. J. Therm. Anal. Calorim. **69**, 1031–1036 (2002)
26. Gangadhara Rao, M.V.B.B., N., S.D.: A generalized Relationship to estimate thermal resistivity of soils. Can. Geotech. J. 36, 767–773 (1999)
27. Marotta, E.E., Fletcher, L.S.: Thermal contact conductance for Alumimum and Stainless steel contacts. J. Thermophys. Heat Transf. **12**(3), 374–381 (1998)
28. Mirmira, S.R., Jackson, M.C., Fletcher, L.S.: Effective thermal conductivity and thermal contact conductance of graphite fiber composites. J. Thermophys. Heat Transf. **15**(1), 18–26 (2001)
29. Kumar, S.S., Abilash, P.M., Ramanurthi, K.: Thermal contact conductance for cylindrical and spherical contacts. Heat Mass Transf. **40**, 678–688 (2004)
30. Sridhar, M.R., Yovanovich, M.M.: Elastoplastic contact conductance model for isotropic conforming rough surfaces and comparison with experiments. J. Heat Transf. **118**(1), 3–9 (1996)
31. Farouki, O.T.: Thermal design considerations in Frozen Ground Engineering. In: Krzewinski, T.G., Rupert, G., Tart, J. (eds.) p. 277. ASCE, New York (1985)
32. Hadley, G.R.: Thermal conductivity of packed metal powders. Int. J. Heat Mass Transf. **29**(6), 909–920 (1986)
33. Becker, B.R., Misra, A., Fricke, B.A.: Development of correlations for soil thermal conductivity. Int. Commun. Heat Mass Transf. **19**, 59–68 (1992)
34. Gavriliev, R.I.: Thermal properties of soils and surface covers. In: Reston, D.C. (ed.) Thermal analysis, construction, and monitoring methods for frozen ground, vol. 492, pp. 277–294, ASCE, VA (2004)
35. Andersland, O.B., Ladanyi, B.: Frozen Ground Engineering. 2 ed. Hoboken, p. 363. Wiley, NJ, ASCE (2004)
36. DeVera, A.L., Strieder, W.: Upper and lower bounds on the thermal conductivity of a random, two-phase material. J. Phys. Chem. **81**(18), 1783–1790 (1977)
37. Sass, J.H., Lachenbruch, A.H., Munroe, R.J.: Thermal conductivity of rocks from measurements on fragments and its application to heat-flow determination. J. Geophys. Res. **76**(14), 3391–3401 (1971)
38. Hashin, Z., Shtrikman, S.: A variational approach to the theory of the effective magnetic permeability of multi-phase materials. J. Appl. Phys. D: Appl. Phys. **33**(10), 3125–3131 (1962)
39. Hill, R.: A self-consistent mechanics of composite materials. J. Mech. Phys. Solids **13**(4), 213–222 (1965)
40. Gori, F., Corasaniti, S.: Theoretical prediction of the thermal conductivity and temperature variation inside Mars soil analogues. Planet. Space Sci. **52**, 91–99 (2004)